



# Multi-stage mechanical behavior and damage mechanism of composite interference-fit joints subject to long-term low-temperature aging

Jian Li<sup>1,2,3</sup> · Wei Guo<sup>2</sup> · Peng Zou<sup>4</sup> · Zhihui Zhou<sup>1</sup> · Yibiao Fan<sup>2</sup>

Received: 19 February 2023 / Accepted: 21 August 2023 / Published online: 27 October 2023  
© The Author(s), under exclusive licence to The Brazilian Society of Mechanical Sciences and Engineering 2023

## Abstract

Carbon fiber-reinforced polymer (CFRP) composite joint structures based on interference fit exhibit superior mechanical properties compared to equivalent joint geometries utilizing clearance fits. The present research investigates the mechanical properties and failure mechanism of CFRP interference-fit joints subject to long-term exposure to low temperatures. A series of studies were designed to examine with interference-fit sizes ranging from 0 to 2.11%, subjected to temperatures between  $-60$  and  $20$  °C, and aging periods from 0 to 18 months. Tensile tests were conducted on these samples. Using a microscale analysis, three-dimensional representative volume elements (3D-RVEs) models were constructed to analyze the internal state, distribution of thermal residual stress, and damage initiation mechanism of CFRP subjected to low-temperature exposure. The results show that the strength and stiffness of the CFRP joints initially increase, reach a peak, and subsequently decrease with an increase in either the interference-fit size or aging time. The strength and stiffness of the considered geometries exhibit an approximately linear increase with decreasing temperature. Inside the CFRP, exposure to low temperatures causes the formation of thermal residual stress, which is particularly high in areas with closely spaced fibers. Short-term low temperature enhances the bonding force between the fiber and matrix, thereby improving the mechanical properties of the CFRP interference-fit joint structures. Following prolonged exposure to low temperatures, the debonding cracks formation increase in regions with concentrated residual stress, thereby decreasing the strength and stiffness of the structure.

**Keywords** Long-term low-temperature exposure · Interference-fit · Thermal residual stress · Crack propagation · Damage mechanism

---

Technical Editor: João Marciano Laredo dos Reis.

✉ Jian Li  
leejian@lyun.edu.cn

- <sup>1</sup> Powder Metallurgy Research Institute, Central South University, Changsha 410006, China
- <sup>2</sup> Fujian Provincial Key Laboratory of Welding Quality Intelligent Evaluation, Longyan University, Longyan 364012, China
- <sup>3</sup> Hangzhou Yitong New Materials Co., Ltd, Hangzhou 311600, China
- <sup>4</sup> National Key Laboratory of Strength and Structural Integrity, Aircraft Strength Research Institute of China, Xi'an 710065, Shaanxi, China

## 1 Introduction

Due to their low weight, high specific strength, high specific stiffness, corrosion resistance, and fatigue resistance, carbon fiber-reinforced polymer (CFRP) composites joints are widely utilized in the fields of aviation, railway, automotive, and civil engineering [1, 2]. However, one of the significant environmental factors that frequently affect CFRPs during their service life is low temperatures. Specifically, CFRP joints used in applications related to high-altitude flight, alpine environments, and winter conditions at high latitudes often experience prolonged exposure to low-temperature environments. Consequently, the performance of CFRP joints is influenced by the behavior of CFRPs at low temperatures [3, 4].

Currently, research on the mechanical properties of CFRP laminates in low-temperature environments primarily focuses on the ultra-low-temperature regime, where the

strength of the composite material is significantly enhanced compared to its strength at room temperature [5]. However, due to the different thermal expansion coefficients of the epoxy (EP) resins and fibers in CFRPs, debonding at the interface between the matrix and the fibers can occur, resulting in the formation of interfacial microcracks that affect the mechanical properties of the composite material [6, 7]. Limited research is available on the mechanical characteristics of CFRP in the temperature range from 0 to  $-60$  °C. The bending characteristics of CFRPs were investigated by Zaoutos et al. [8] for materials exposed to a temperature of  $-40$  °C for various time periods (30, 45, and 60 days). This work examined the impact of freezing cycles on the mechanical properties. Wilson et al. [9] demonstrated that in the temperature from 0 to  $-80$  °C, the internal stress of the material increases, causing the formation of microcracks in the carbon fiber (CF)/EP composite laminates. It was found by Dutta et al. [10] that, while the tensile strength of glass fiber composites was improved in  $-40$  °C and  $-60$  °C, the crack propagation that occurred during thermal cycling resulted in a considerable reduction in the mechanical behavior of the material by long-term low-temperature exposure. The mechanical properties of fiber-reinforced resin matrix composites under exposure to low temperatures were investigated by Takeda et al. [11, 12]. A microscale analysis was employed to investigate the accumulation of damage occurring at low temperatures and the failure mechanism of the composites. Furthermore, numerical modeling techniques have been utilized to examine the distribution of residual stress in composite materials subsequent to low-temperature exposure [13–17]. Qi Wu et al. [18–20] undertook finite element (FE) simulations using representative random models and large-scale parallel computing; this work simulated the formation of residual stresses based on the mesoscopic scale. Solati et al. [21–23] have made noteworthy contributions to the understanding of bearing response and damage mechanisms in FRP composites and their joints. Through a combination of experimental investigations and finite element analysis, they have uncovered crucial information regarding surface quality, mechanical properties, and failure models of FRP materials. These findings provide valuable insights for the simulation analysis of FRP materials. Combining experimental and FE techniques, Li et al. [24] created a RVE model with random fiber distribution. They investigated the transverse tensile properties of composites exposed to low temperatures.

Nowadays, the research focus on the low-temperature characteristics of CFRPs primarily revolves around evaluating their performance at specific low temperatures, with a particular emphasis on CFRP laminates. However, there is limited work on the long-term performance of CFRP subjected to a range of low-temperature conditions; little work exists in the literature investigating the behavior of

interference-fit joints. Existing research indicates that the use of interference fits can improve the mechanical properties of the connector [25–28]. The mechanical performance of CFRP interference-fit joints is affected by long-term exposure to a low-temperature environments. Given the widespread use of CFRPs, conducting an in-depth investigation into the effect of low temperatures on this material and its joints is essential. Therefore, it is crucial to examine the mechanical characteristics and damage process of interference-fit geometries in CFRP joints that are exposed to low temperatures over an extended period of time.

In this paper, we investigated the tensile mechanical properties of CFRPs interference-fit joints that were subjected to long-term exposure to low-temperature environments by simulating the low-temperature environment in the laboratory. To achieve this, three-dimensional multiphase microscale models of CFRP material were created using FE analysis software, and the models were employed to examine the internal mechanical response and damage behavior of the fiber/matrix composite in a low-temperature environment.

Moreover, we aim to elucidate the evolution of the mechanical properties and the failure mechanism of CFRP joints. This study plays a critical role in ensuring the durability and safety of interference joints in CFRPs exposed to low temperatures.

## 2 Experimental methodology

### 2.1 Specimen preparation

The CFRP composite laminates investigated in this study were fabricated using the vacuum bag molding process. CF prepreg (T700) with a thickness of 0.2 mm per ply was employed as the reinforcement; while polyester resin 9916 was served as the matrix. The composites were constructed with a layup configuration of  $[0^\circ/\pm 45^\circ/90^\circ]_{2s}$ , resulting in the finished laminates with a thickness of 3.2 mm and composed of 16 plies. The laminate exhibited a fiber volume content of 65%.

The CFRP laminates were cut into rectangle specimens, and holes were drilled in the specimen using a computer numerical control (CNC) machine. The dimensions of the specimens are shown in Fig. 1. A coated four-blade dagger drill specifically designed for use with composite materials was utilized to obtain holes with diameters of 6.35 mm. The machining accuracy was to within  $\pm 0.004$  mm. Two CFRP specimens were stacked and fastened together prior to the drilling procedure to prevent relative motion between the two specimens. The stacked drilling technique was used to ensure consistency between the top and lower plate apertures. The bolts were Ti-alloy Hi-Lok fasteners (provide by Oriental Bluesky Titanium Technology Co., Ltd, China)

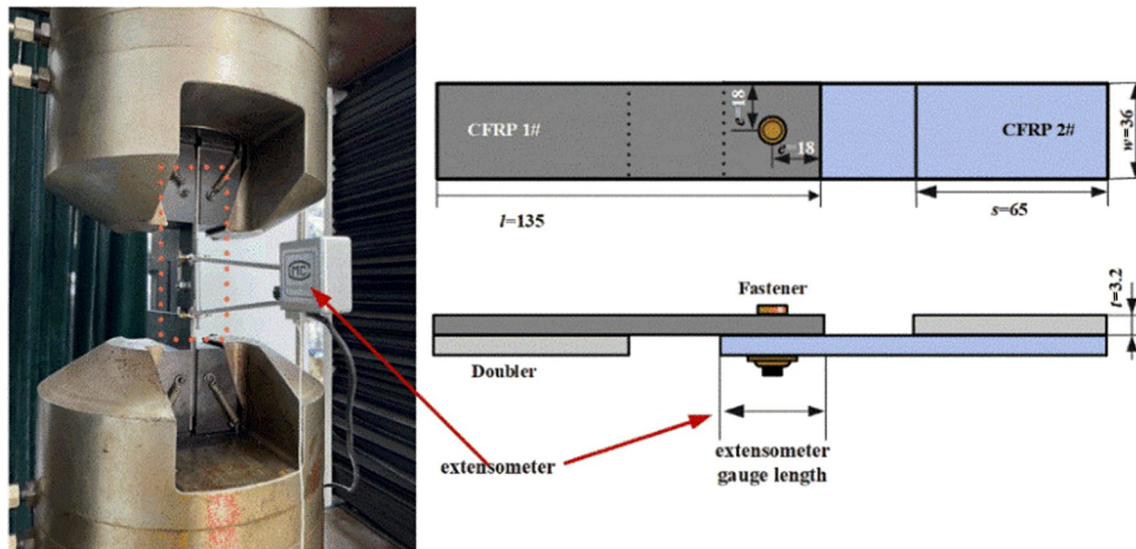


Fig. 1 Geometry and configuration of the CFRP interference-fit joint (unit: mm)

produced with a machining precision of less than  $\pm 0.01$  mm. Prior research has demonstrated that interference-fit joints benefit from the application of a 4 Nm torque to increase tensile strength [26]. Thus, the nuts and flats were prepared individually to replace the original nuts, and a torque wrench was used to increase the torque applied to each connector to 4 Nm (compared with 2.36 Nm that was applied to the original nuts). The diameters of the shank of the bolts were intended to be 6.4 and 6.5 mm. The diameters of each hole and bolt shank were measured, so the proper interference fit sizes were achieved by size calculation. Then, the matching of hole–shank diameters was performed so that the specimens could be assembled utilizing the appropriate interference-fit sizes: 0.54%, 0.74%, 1.15%, 1.64%, and 2.11%.

### 2.2 Mechanical testing

To study the effect of long-term exposure of CFRP interference joints to low temperatures, we examined the performance of various specimens at temperatures of 20 °C, 0 °C, –20 °C, –40 °C, and –60 °C, along with exposure times of 0, 1, 6, 12, and 18 months. The test pieces were placed in a series of test chambers set to different temperatures (the temperature range achievable in the test chamber is –60 °C to 150 °C, the temperature fluctuation is  $\leq \pm 0.5$  °C, and the temperature deviation is  $\leq \pm 3$  °C). The cooling rate used here was 2 °C/min. When the temperature reached the desired value, the temperature was held for the duration specified in Table 1; the number of specimens used in each group was not less than 3.

The test pieces were removed from the long-term low-temperature treatment and left to reach ambient temperature (20 °C) naturally. Tensile tests were then undertaken on the

Table 1 Test conditions for each test group

No.	Temperature/°C	Time/m	Interference-fit
A-1	20	12	1.15%
A-2	0	12	1.15%
A-3	–20	12	1.15%
A-4	–40	12	1.15%
A-5	–60	12	1.15%
B-1	–60	12	Clearance fit
B-2	–60	12	0.54%
B-3	–60	12	1.15%
B-4	–60	12	1.64%
B-5	–60	12	2.11%
B-1	–40	0	0.74%
B-2	–40	1	0.74%
B-3	–40	6	0.74%
B-4	–40	12	0.74%
B-5	–40	18	0.74%
B-6	–40	0	1.64%
B-7	–40	1	1.64%
B-8	–40	6	1.64%
B-9	–40	12	1.64%
B-10	–40	18	1.64%
B-11	–40	0	2.11%
B-12	–40	1	2.11%
B-13	–40	6	2.11%
B-14	–40	12	2.11%
B-15	–40	18	2.11%
C-1 (90° ply)	–40	1	1.15%
C-2 (0° ply)	–40	1	1.15%

test pieces using a INSTRON universal testing machine. During the tensile loading, the samples were loaded using a displacement control technique at the rate of 1.5 mm/min. A displacement extensometer was placed on the sample and bearing tests were performed according to ASTM D5961 standard, as shown in Fig. 1.

### 3 Numerical simulations

Directly evaluate the change in thermal residual stress and the damage initiation behavior of CFRP samples during tensile process after exposure to low temperatures is difficult. Therefore, it is therefore necessary to perform numerical simulations on a microscopic scale to evaluate the residual stress distribution within a CFRP part subject to low-temperature environments. However, for accurately depicting the micromechanical response of CFRPs, however, it is necessary to consider the random nature of the fiber distribution within the material, the fiber volume fraction, the number of fibers in a RVE, and the minimum model size.

The thermal residual stress and tensile failure behavior of the CFRP composites after low-temperature exposure were simulated using the commercial FE analysis program ABAQUS/Explicit 2022. A three-dimensional RVE model can be utilized to analyze these behaviors of the samples after being exposure to low temperatures. For the low-temperature thermal residual stress, the 3D-RVE model is established in the simulation initially, and a transient thermal analysis step is then set up to calculate the thermal residual stress generated inside the CFRP micro-model from room temperature to  $-40\text{ }^{\circ}\text{C}$ . Subsequently, the thermal residual stress field was used as the initial state of the RVEs model for the tensile damage analysis at low temperature. The VUMAT subroutine was used to model the accumulation of damage within the fibers and matrix. A vertical tensile load was then applied to the RVE model to evaluate of the damage post-loading.

#### 3.1 Description of the 3D RVE model

We utilized a combined continuum–discrete three-dimensional microscale FE model with fiber, matrix, and cohesive elements at the fiber–matrix interface to investigate the mechanical response of the CFRP samples after low-temperature exposure. Specifically, we investigated the damage initiation and damage propagation behavior of the material. Traditionally, generating a three-dimensional RVE model that meets the necessary criteria for evaluation in ABAQUS requires manual design. However, in this work, it was necessary to model a large number of fibers and consider the random distribution of fibers, as well as high fiber volume fractions. To address these requirements, Python was employed

to automatically generate a suitable three-dimensional RVE model. Furthermore, periodic boundary conditions were implemented within the RVE model to accurately capture the behavior of the CFRP.

The residual stress analysis is mainly related to scalars such as the thermal expansion coefficients of fibers and matrix in the RVE model, and it is independent of the fiber orientation angle. Therefore, in this paper, only the  $90^{\circ}$  ply is analyzed for thermal residual stresses. On the other hand, during the loading process, the micro-damage in the RVE model is related to the loading direction, fiber orientation angle, and other factors. As a result, subsequent analyses of the RVE model with different fiber orientation angles are conducted in the subsequent micro-damage process.

Figure 2 shows the 3D RVE model used in ABAQUS (the CFs are represented by cylinders). The fiber volume fraction in the modeled material is 65%, the fiber radius is  $7\text{ }\mu\text{m}$ . In order to analyze the failure modes of different layers and reduce the calculation of the models, two sizes of RVEs are established. The dimensions of the 3D RVE are  $150 \times 150 \times 20\text{ }\mu\text{m}$  and  $200 \times 100 \times 30\text{ }\mu\text{m}$ . The EP matrix is distributed around the fiber, and an interface layer is defined between the matrix and the fiber. Solid elements C3D8R (8-node linear hexahedron element with enhanced hourglass control reduced integration) in a three-dimensional stress state are used to model both the CF and resin matrix, and the fiber–matrix interface modeled using zero-thickness cohesive elements that shares the existing nodes defined by the mesh used to define the fiber and matrix elements. An element mesh size of  $0.7\text{ }\mu\text{m}$  is defined for the global seed layout to improve the calculation accuracy.

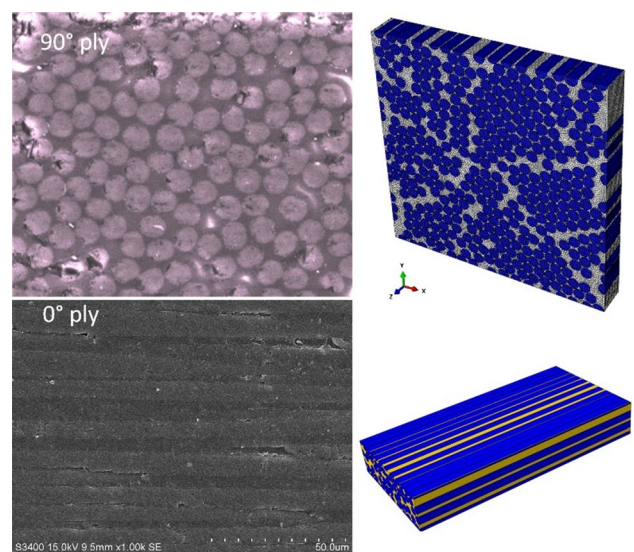


**Fig. 2** Partial scanning electron microscope (SEM) image and 3D-RVEs model of the CFRP

Because CFRP has the weakest bearing capacity in the direction perpendicular to the fiber, the cracks initially occurred in the plyer that fiber was oriented at 90° to the direction of the applied tension loading. As the imposed displacement increased (applying tension to the sample), the crack propagated toward the interlayer, causing delamination and, eventually, failure.

The mechanical interaction between the shank of the bolt and the workpiece is modeled using a “penalty contact” approach considering Coulomb friction. The penalty contact is applied to all the elements within the workpiece to prevent inter-element penetration, which, by default, is not taken into account before element deletion. The coefficients of friction between the bolt shank and the RVE, and between the fiber and the matrix, are set to be 0.2 [29] and 0.5 [30], respectively.

### 3.2 Materials model

#### 3.2.1 Continuum damage model for CF and EP matrix

The CF is assumed to be a linearly elastic and transversely isotropic material in this model. When the elemental stress exceeds the defined strength in a given direction, the CF will experience fails. This simplifies the modeling process and accurately describes the experimentally reported mechanism of fiber fracture [31, 32].

In this paper, the maximum stress failure criterion was adopted, and the criteria are described in Table 2.

In the case of elements representing the CF, when the elemental stress  $\sigma_{11}$  within an element reaches the tensile strength (defined as  $X_t$ ), the value of the damage variable  $d_{t1}^f$  is set to unity, representing the maximally damaged state. When this condition is met,  $\sigma_{11}$  is reduced to zero instantaneously, and the corresponding element is deleted. This behavior is applied to all elements representing the fibers. The compression failure is assumed to be more sudden to reduce the computing time.

To simulate the mechanical response of the CFRP in a low-temperature environment, it is also essential to define the mechanical properties of the material, including material density, thermal expansion coefficient, strength, modulus, and Poisson’s ratio. The material properties utilized here are shown in Table 3. The constitutive behavior of the EP matrix is assumed to be isotropic and elastoplastic. The predefined Johnson–Cook constitutive model is employed to describe the yielding behavior of the matrix; this model is described in Table 3.

The thermal expansion coefficients of the fiber and the resin are different; this affects the mechanical properties of the matrix [33]. We note that because the material properties of polyester EP resin 9916 used here are not available in the literature, we model this resin using the parameters that describe a resin with similar properties (EP resin E–51).

#### 3.2.2 Discrete damage model for the fiber–matrix interface

The interface between fiber and matrix is modeled using zero-thickness cohesive elements (COH3D8), and the behavior of the elements is defined by a traction–separation law. The initial response is assumed to be linear, with the slope representing the elastic stiffness ( $K = 10^5 \text{ N/mm}^3$ ). A high value of  $K$  is used in all three directions to prevent penetration of the interfaces. The constitutive relation for pure tension (mode I) or pure shear loading (mode II) is presented in Fig. 3 [34].

Cohesive damage is assumed to initiate when

$$\left(\frac{t_n}{t_n^0}\right)^2 + \left(\frac{t_s}{t_s^0}\right)^2 + \left(\frac{t_t}{t_t^0}\right)^2 = 1 \tag{1}$$

Mixed-mode, progressive damage is defined based on the interaction of the fracture energies using the Benzegagh–Kenane fracture criterion [35], which is defined by,

$$G_1^C + (G_2^C - G_1^C) \left(\frac{G_2 + G_3}{G_1 + G_2 + G_3}\right)^\eta = G^C \tag{2}$$

where  $\eta$  is a mixed-mode parameter.

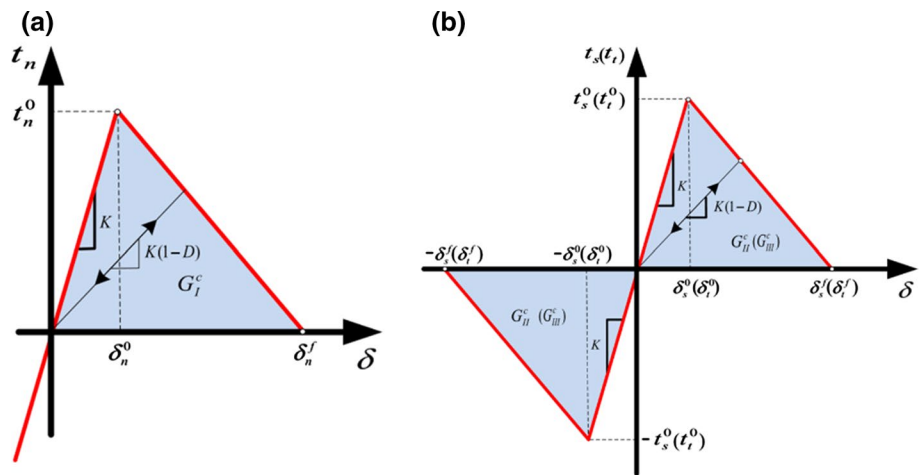
**Table 2** Control criterion for the initiation of damage

Maximum stress criterion	Described formulation
Tensile loading in longitudinal direction	$d_{t1}^f = \sigma_{11}/X_t, \sigma_{11} \geq 0$
Compressive loading in longitudinal direction	$d_{c1}^f =  \sigma_{11}/X_c , \sigma_{11} < 0$
Tensile loading in transverse direction	$d_{t2}^f = \sigma_{22}/Y_t, d_{t3}^f = \sigma_{33}/Y_t; \sigma_{22} \geq 0 \text{ or } \sigma_{33} \geq 0$
Compressive loading in transverse direction	$d_{c2}^f =  \sigma_{22}/Y_c , d_{c3}^f =  \sigma_{33}/Y_c ; \sigma_{22} < 0 \text{ or } \sigma_{33} < 0$
Shear loading in plane	$d_{s12}^f =  \tau_{12}/S $
Shear loading out of plane	$d_{s23}^f = \max( \tau_{13}/S ,  \tau_{23}/S )$

**Table 3** The thermal/mechanical properties of the CFRP

Material	Property	Values
T700 fiber	Elastic constants	$E_{11} = 230 \text{ GPa}, E_{22} = E_{33} = 14 \text{ GPa},$ $\nu_{12} = \nu_{13} = 0.2, \nu_{23} = 0.25,$ $G_{12} = G_{13} = 24 \text{ GPa}, G_{23} = 5.5 \text{ GPa},$
	Tensile strength	$X_t = 4620 \text{ MPa}, Y_t = 1500 \text{ MPa}$
	Compressive strength	$X_c = 3960 \text{ MPa}, Y_c = 3340 \text{ MPa}$
	Shear strength	$S = 1500 \text{ MPa}$
	Thermal expansion coefficient	$\mu_{axi} = -3.8e^{-7} \text{ m/mK}, \mu_{rad} = 7e^{-6} \text{ m/mK}$
Epoxy resin E-51	Elastic constants	$E_{mh} = 3 \text{ GPa}, E_{ml} = 4.4 \text{ GPa}, \nu_m = 0.35, G_m = 1.1 \text{ GPa}$
	Yield strength	$\sigma_{y0}^m = 120 \text{ MPa}$
	Johnson–Cook Parameters	$A = 120 \text{ MPa}, B = 654.18 \text{ MPa}, n = 0.772, c = 0.124, m = 0.304$
	Thermal expansion coefficient	$\mu_m = 1.24e^{-4} \text{ m/mK}$
Interface	Fracture energy	$G_m^C = 0.1 \text{ N/mm}, G_1^C = 0.002 \text{ N/mm}, G_2^C = G_3^C = 0.006 \text{ N/mm}$
	Normal strength	$t_n = 50 \text{ MPa}$
	Shear strength	$t_s = 75 \text{ MPa}$
	Elastic stiffness	$K = 100,000 \text{ N/mm}^3$
	Mixed-mode parameter	$\eta = 1.45$

**Fig. 3** The traction–separation response of a zero-thickness cohesive element: the response of the element to **a** normal loading and **b** shear loading



## 4 Results and discussion

### 4.1 Effect of exposure to low temperatures

On a macroscopic scale, the types of failure observed in the specimens exposed to various low temperatures are similar to those observed at ambient temperature (fiber and matrix fracture as well as delamination); however, the displacements in the joint area differed between the two sets of samples subject to given load, as shown in Fig. 4.

The microscopic failure of the joints did not change significantly due to the low-temperature environment in the experiment, which primarily induces physical changes [36]. We note that it has been established that ultra-low temperatures can damage the molecular structure of the

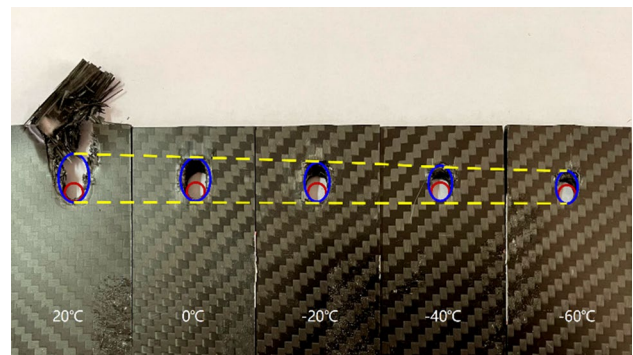


**Fig. 4** Failure morphology of tensile test specimens subject to different temperatures

resin matrix. The displacement of the shank-hole in the bolted joint decreases when subject to low temperatures, which means the stiffness of the bolted joint increases in this regime.

### 4.1.1 Interference fits

Due to the difference in thermal expansion coefficients of the fibers and the resin matrix, thermal residual stresses are induced in the material when the temperature of the sample is varied. These residual stresses can affect the stress transmission between the fibers and matrix when the CFRP interference-fit bolted joint is loaded, thereby impacting the overall mechanical properties of the structure.

Figure 5 presents the load–displacement curves of the CFRP single lap interference-fit bolted joints under tension after a 12-month exposure to temperatures of  $-40\text{ }^{\circ}\text{C}$  with different interference-fit geometries. As illustrated in Fig. 5a, there is a “sliding stage” is observed in the case of

the clearance-fit bolted joint, where the bolt slips within the hole when the tensile load surpasses the friction generated by the preload. This occurs because the bolt slips in the hole when the tensile load exceeds the friction created by the preload. The interference-fit bolted joint enters a “transition stage”, primarily due to the buckling fracture behavior of some of the fibers in the region close to the interference fit, resulting in a significant change in the slope of the tensile curve during the loading process. This regime demonstrates a decrease in the stiffness of the structure. Figure 5b shows the ultimate tensile strength of the interference-fit joints designed with different interference sizes at low temperatures. The ultimate tensile strength exhibits a peak at a specific interference-fit size. In this work, the maximum tensile strength was observed for an interference-fit size of 1.64%.

The stiffness of the interference-fit joint will also be affected by long-term exposure to low temperatures. The stiffness of the interference-fit joint is calculated here using a displacement extensometer. As shown in Fig. 5c, the

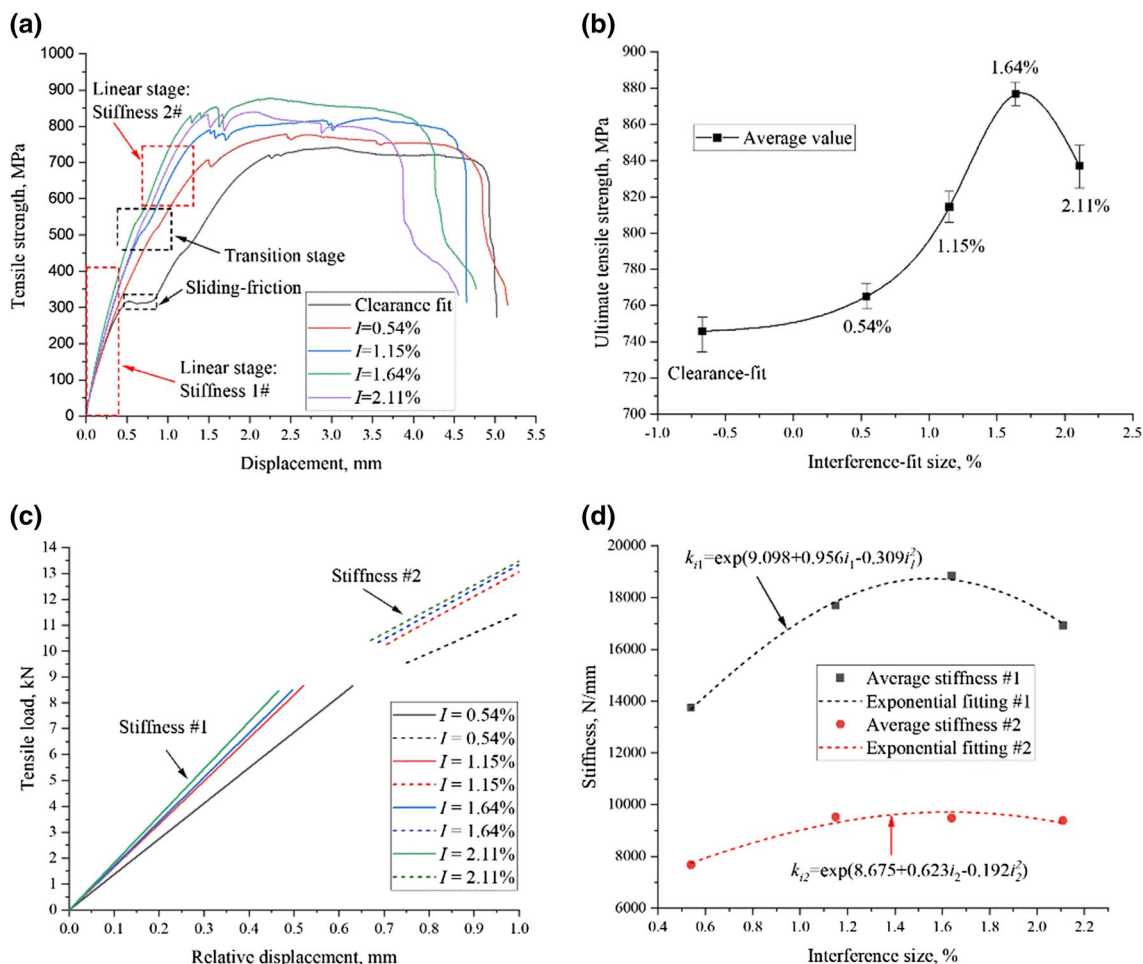


**Fig. 5** The variation of the strength and stiffness of CFRP bolted joint for different interference-fit sizes after a 12-months exposure to low temperatures: **a** A typical load–displacement curve, **b** ultimate tensile

strength for different interference-fit sizes, **c** typical stiffness curves, and **d** fitting of stiffness data

gradient of the load–displacement curve for the interference-fit joints changes during the tensile loading process. This change allows us to define two regimes, namely, the initial stage (referred to here as the interference-fit stage or S1) and the second stage (here, referred to as the non-interference fit stage or S2). These stages are separated by a “transition stage”. The gradient observed in S1 is significantly larger than that observed in S2. Figure 5d shows the stiffness change and the fitting of the stiffness curves describing the behavior of the joints after long-term low-temperature exposure. It can be observed that the stiffness in the interference-fit stage is larger than that observed in the non-interference stage, and with increasing interference-fit size, the stiffness first increases and then decreases.

The equivalent stiffness is used for calculating the stiffness of the bolted joint in engineering, which considers the coordination between the bolt and plate stiffnesses. However, in the engineering design process, a safety factor of 1.5 is typically applied to the bolted joint in the case of “load and pre-tightening”. According to the standard calculations, the allowable stress of the bolted joint occurs during the S1 stage. Therefore, calculating the equivalent stiffness has little significance. As a result, we focus on the stiffness of the S1 regime and derive an expression to calculate the stiffness of interference-fit joints through nonlinear fitting of the data obtained from samples exposed to long-term low temperatures; this expression is given by,

$$k_{i1} = \exp(9.098 + 0.956i_1 - 0.309i_1^2) \quad (3)$$

where  $i$  is the interference-fit size.

#### 4.1.2 Temperature

The temperature has an impact on the mechanical properties of CFRP interference-fit bolted joints. As the temperature decreases, the resin matrix within the CFRP undergoes shrinkage, leading to increased intermolecular bonding forces, and stronger bonding at the resin-fiber interface. Consequently, the tensile strength of the CFRP material steadily increases. This observation aligns with previous literature findings where bolted joints with an interference-fit size of around 1% ~ 1.5% demonstrate excellent mechanical properties [23]. In this study, we specifically examine the effects of exposures to different temperatures on the specimens with an interference-fit size of 1.15% within the temperatures range of 20 °C to –60 °C. Figure 6 illustrates the mechanical properties of the interference joint after 12 months of low-temperature exposure. The ultimate tensile strength gradually increases and follows a roughly linear trend as the temperature decreases, as shown in Fig. 6a, b. However, the ultimate strength remains constant over long-term low-temperature exposure. Notably, the ultimate tensile strength at –60 °C is

7.3% higher than at 20 °C. This enhancement is attributed to the potential formation of microcracks at the fiber-matrix interface in areas experiencing significant thermal residual stress due to long-term low-temperature exposure. The linear fitting equation for the strength of an interference bolted joint at different temperatures is as follows:

$$S = 824.7 - 0.783t \quad (4)$$

where  $t$  is the temperature.

Figure 6c, d shows the evolution of the stiffness of the CFRP as a result of exposure to different temperatures. In the case of various long-term low-temperature treatments, a “transition stage” emerges due to the material and interference-fit characteristics. The stiffness of a CFRP interference-fit bolted joint can also be divided into two parts, namely S1 and S2. The decline in stiffness resulting from temperature follows an approximately linear trend. Notably, the stiffness of the structure within the S1 regime exhibited a 33% increase as temperature decreased to –60 °C over 12-months period (see Fig. 6d). Conversely, the stiffness of the structure within the S2 regime increased by 12.8%. This observation suggests that the impact of low-temperature exposure on stiffness is more pronounced compared to its effect on the strength of the interference joint. Through linear fitting, we obtained an expression for the stiffness of the component in the S1 regime:

$$k_{i1} = 19451.6 - 82.1t. \quad (5)$$

#### 4.1.3 Aging time

The duration of the exposure to low temperatures also has an impact on the mechanical properties of the CFRP and the joint. Figure 7 illustrates the variations in the tensile strength and stiffness of the CFRP interference-fit bolted joint after being subjected to temperatures of –40 °C for different lengths of time. Figure 7a displays the load–displacement curve following various durations of low-temperature treatment. The tensile strength initially increases and subsequently decreases over time. Figure 7b presents the ultimate tensile strength of the joints in relation to time and interference-fit sizes. It is evident that the ultimate tensile strength undergoes significant variations within the first 6 months and gradually diminishes over time. Notably, the specimens exhibit the most rapid increase in strength after the first month of exposure to low temperatures. This observed strength increase can be attributed to the shrinkage of the matrix resin and enhanced intermolecular interactions occurring at low temperatures, which improve the bonding between the resin and fibers and effectively enhance the strength of the fibers. Conversely, the subsequent strength decrease is caused by the differential thermal expansion



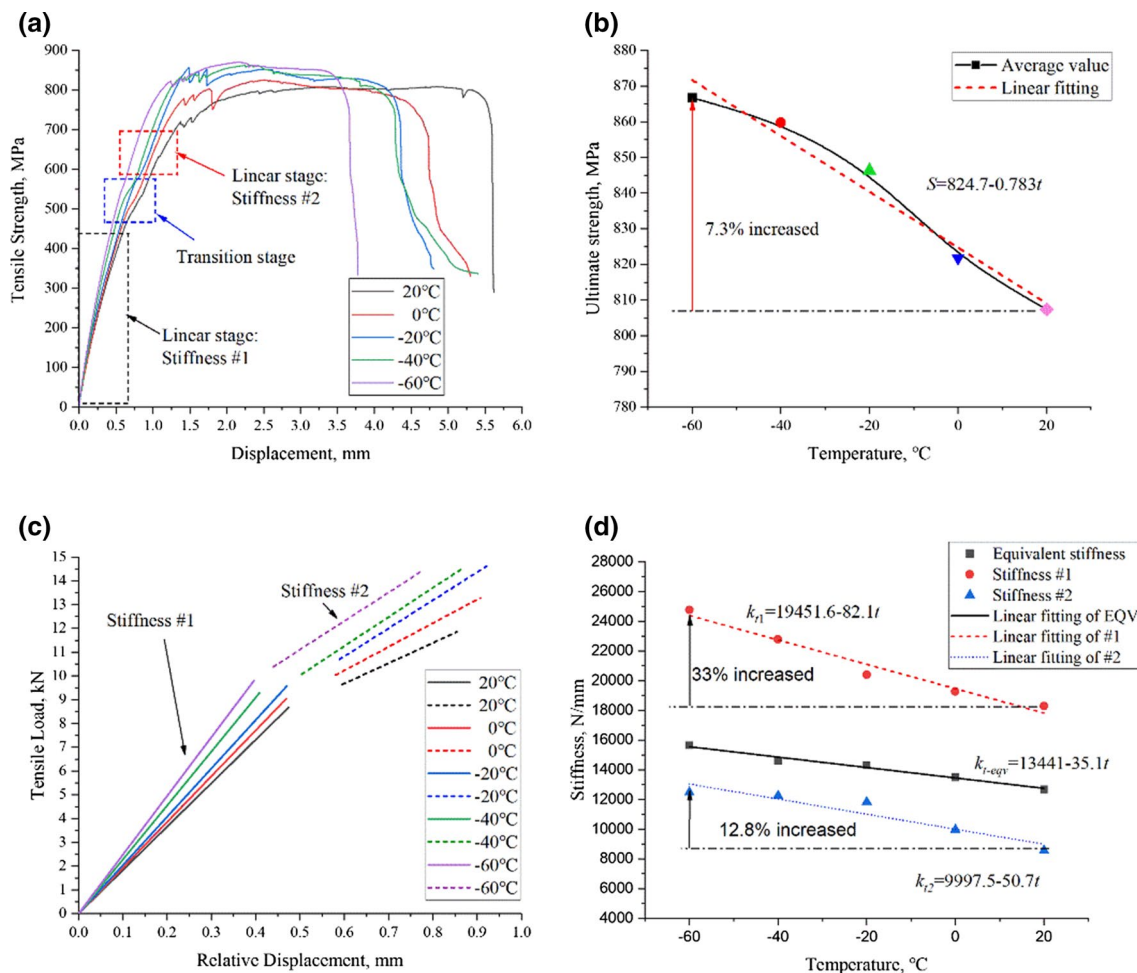


**Fig. 6** Tensile behavior of CFFP interference-fit bolted joints after exposure to low temperatures for 12 months

coefficients between the fibers and the resin matrix. Consequently, after an extended period of low-temperature exposure, the deformation of the resin and the fibers becomes non-identical. The shrinkage stress generated by the resin's resistance to shrinkage may exceed the bonding strength between the resin and fibers, leading to the formation of microcracks due to debonding at the fiber-matrix interface. Under tensile loads, the rapid propagation of these cracks leads to delamination damage within the material, consequently reducing its load transfer capacity and strength.

We also analyzed the change in stiffness in Fig. 7c, d. It can be observed that the stiffness of the joint initially increases and then decreases as the duration of low-temperature treatment time increases. The stiffness shows an increasing trend with larger the interference-fit size, and when the low-temperature treatment is prolonged, the decrease in stiffness becomes more significant. Notably, a longer low-temperature exposure leads to a shorter S2 linear phase. This phenomenon suggests that the prolonged exposure may impact the stability of resin matrix molecules. As

a result, the CFRP resin matrix undergoes embrittlement, accompanied by a reduction in cohesion with the fibers, ultimately leading to a diminished bearing capacity of the joint.

### 4.2 Damage analysis

As the RVEs in our study utilize the maximum stress failure criterion, the accuracy of the model can be verified through a comparative analysis of the maximum load-bearing stress between the experimental results and the 3D-RVEs model. Figure 8 presents this comparison, showing the load-bearing strengths obtained from experiments and simulations. The solid lines in the figure represent the load-displacement curves of three samples after one month of low-temperature treatment, while the dashed line represents the load-time curve obtained from the RVE simulation. Specifically, we compared the results obtained from joints with 0° and 90° ply orientations exposed to -40 °C conditions for a month. The models were carefully designed to closely resemble the single-layer thickness and incorporated parameters such as

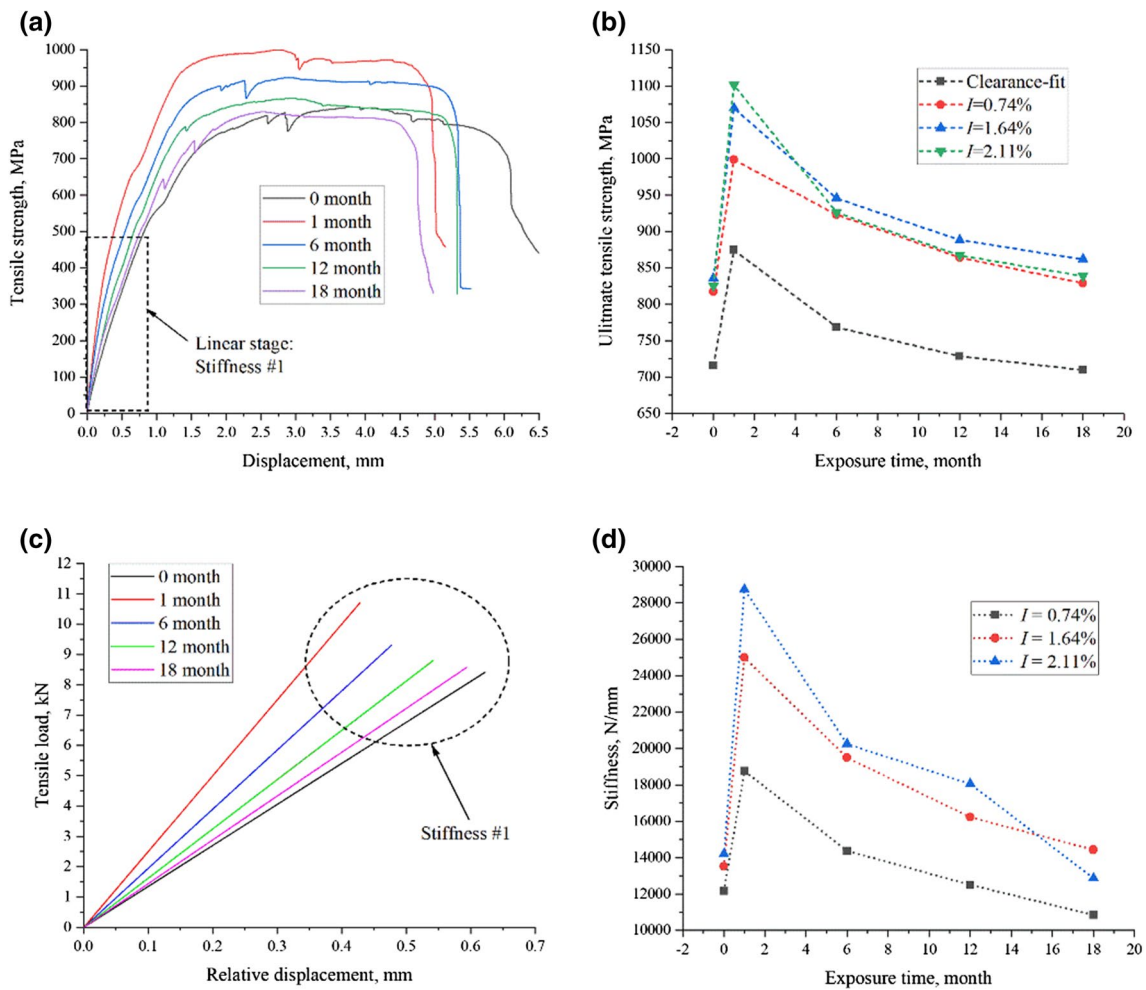


**Fig. 7** The evolution of the strength and stiffness CFRP joints after exposure to temperatures of  $-40\text{ }^{\circ}\text{C}$  for varying durations. **a** Load-displacement curve, **b** Tensile strength of joints subject to low-tem-

perature aging, **c** Values of stiffness #1 subject to low-temperature aging, **d** The change of stiffness with different interference-fit sizes

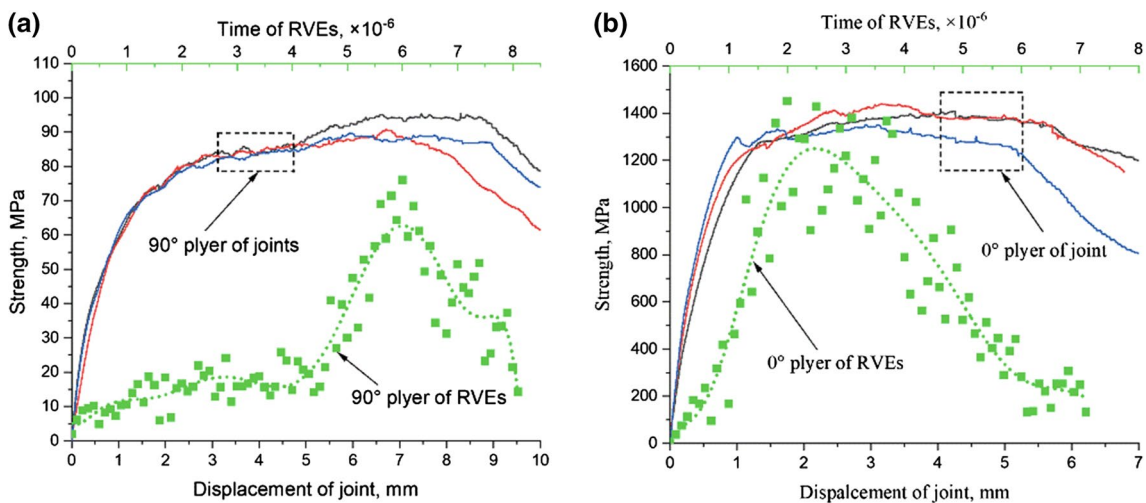


**Fig. 8** Comparison of tensile strength between CFRP interference joints with different pliers and RVEs models; **a** C-1(90° ply) and **b** C-2(0° ply)

random fiber distribution and content that accurately reflect real-world conditions. It is observed that the maximum stress values for different orientations are close to the experimental results. This approach facilitated a meaningful comparison of the maximum load-bearing stress between experimental data and model predictions.

From the data presented in Fig. 8, it is evident that CFRP joints with a  $90^\circ$  ply orientation exhibit a slightly higher (9.5%) maximum load-bearing capacity compared to the maximum stress output obtained from the RVEs. This discrepancy can be attributed to the enhanced interface bonding strength at low temperatures, which was considered in the model through adjustments of the interface bonding parameters. On the other hand, the results of the RVE model slightly exceed the experimental results by 6.5%. This difference can be attributed to the fact that during the experimental process, the load-bearing behavior of the joints involves not only compressive damage but also shear losses occurring in the edge region. These shear losses to some extent diminish the load-carrying capacity. However, the RVE model solely considers compressive damage, leading to slightly higher numerical values compared to the experimental results.

By conducting a comprehensive comparison of the maximum stresses derived from both experiments and the model, the model's effectiveness in analyzing damage behavior is demonstrated. The accuracy of the RVEs model is further substantiated by comparing the failure modes observed in the experiments with those predicted by the model.

#### 4.2.1 Thermal residual stress

In terrestrial applications, exposure to temperatures of  $-40^\circ\text{C}$  is more common than exposure to  $-60^\circ\text{C}$ .

Therefore, the majority of the testing was conducted at  $-40^\circ\text{C}$ . Consequently, an FE analysis was performed to examine the distribution of CFRP thermal residual stress at  $-40^\circ\text{C}$ . In the simulation, the established 3D-RVEs model of the CFRP was utilized to conduct a transient thermal analysis. This analysis aimed to calculate the thermal residual stress generated within the microscale model as the temperature decreased from 20 to  $-40^\circ\text{C}$ . The calculated thermal residual stress distribution in the RVE, resulting from exposure to low temperatures, is presented in Fig. 9. Considering the von Mises stress diagram of the residual stress distribution, it is evident that residual stress is generated in the area where the fibers accumulate.

The coefficient of thermal expansion for fibers is significantly smaller than that of the resin matrix, leading to a mismatch in deformation that results in differing stresses experienced by the fibers and matrix. As evident from Fig. 9, due to the random distribution of fibers, regions with relatively higher fiber content exhibit greater thermal residual stress compared to areas rich in matrix material. Particularly, at the fiber/matrix interface in these two regions, the stress is notably higher than in other areas. This is because the greater matrix content in those regions induces larger stresses caused by low-temperature shrinkage deformation, leading to higher stresses at the fiber/matrix interface.

To further analyze the thermal residual stress in the CFRP by exposure to low temperatures. A pressure-based contour plot to depict the thermal residual stress distribution of fibers and the matrix in Fig. 10. In this representation, positive values indicate tensile stress, while negative values represent compressive stress.

As shown in Fig. 10a, the surface of the fibers experiences both tensile and compressive stresses. Due to the different

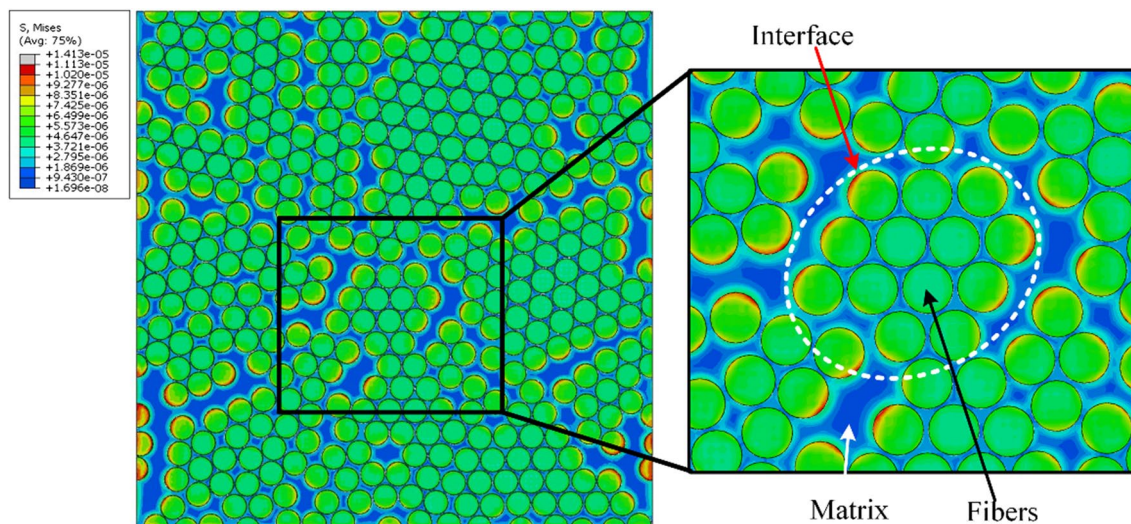
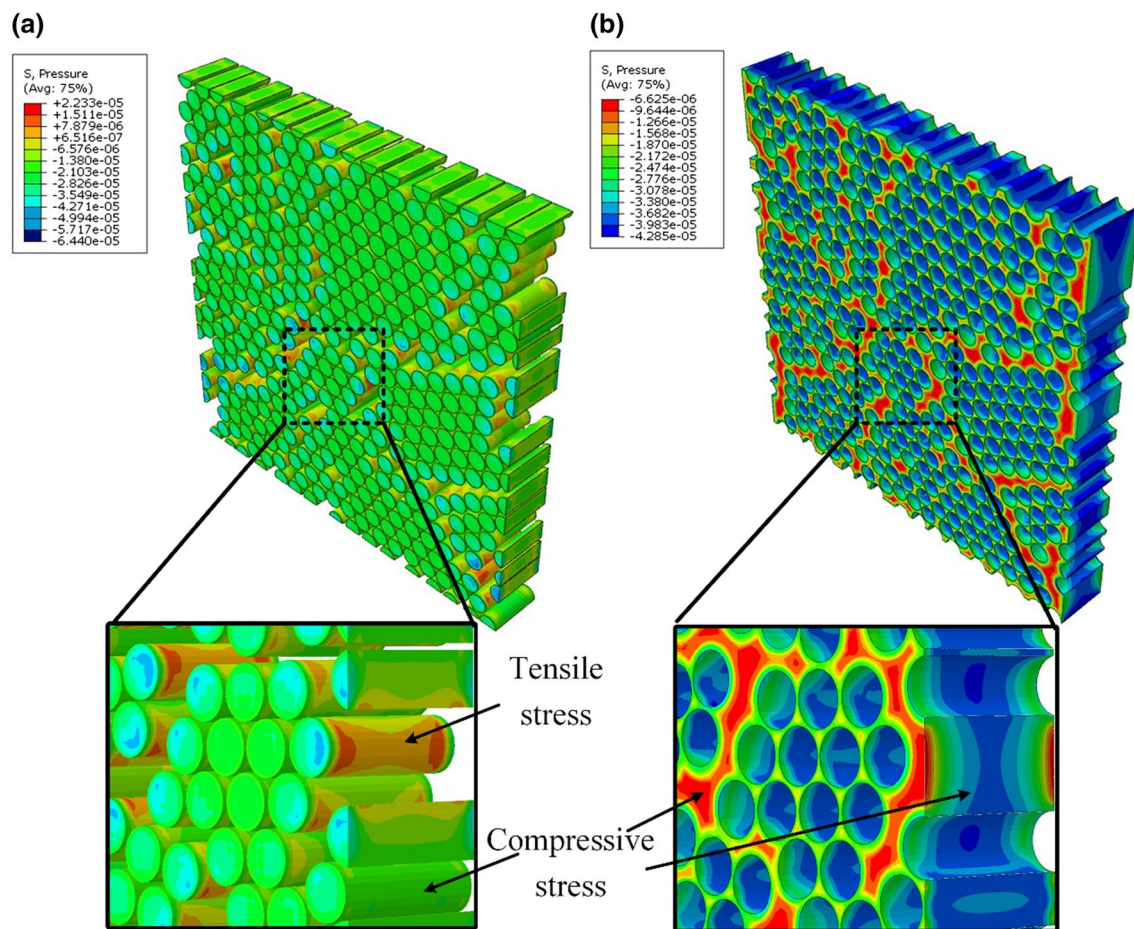


Fig. 9 Residual stress distribution in the CFRP exposure to  $-40^\circ\text{C}$  (unit: TPa)



**Fig. 10** Thermal residual stress distribution in the 3D-RVEs: **a** fibers and **b** matrix

thermal expansion coefficients, the shrinkage of the resin matrix is much larger than that of the fibers. The generation of tensile stress is due to the resistance at the interface during resin shrinkage. On the other hand, compressive stress is produced when the neighboring fibers are squeezed by the resin's contraction in low-temperature environments, particularly noticeable at the fiber/matrix interface in regions where the matrix is abundant and where fibers are enriched.

In Fig. 10b, which illustrates the stress contour plot for the matrix, it can be observed that the matrix experiences compressive stress. This is attributed to the contraction of the matrix as the temperature decreases, resulting in internal compression stresses. In areas where the matrix is more concentrated, higher compressive stresses are generated. Near the fiber/matrix interface, the matrix experiences lower compressive stress. This is because the resin matrix bonded to the fibers will be subjected to tensile stress (interfacial bonding force) to resist the matrix shrinkage, thereby offsetting part of the compressive stress. However, this is not sufficient to alter the overall situation where the matrix experiences compressive stress during low-temperature treatments.

#### 4.2.2 Microscale damage

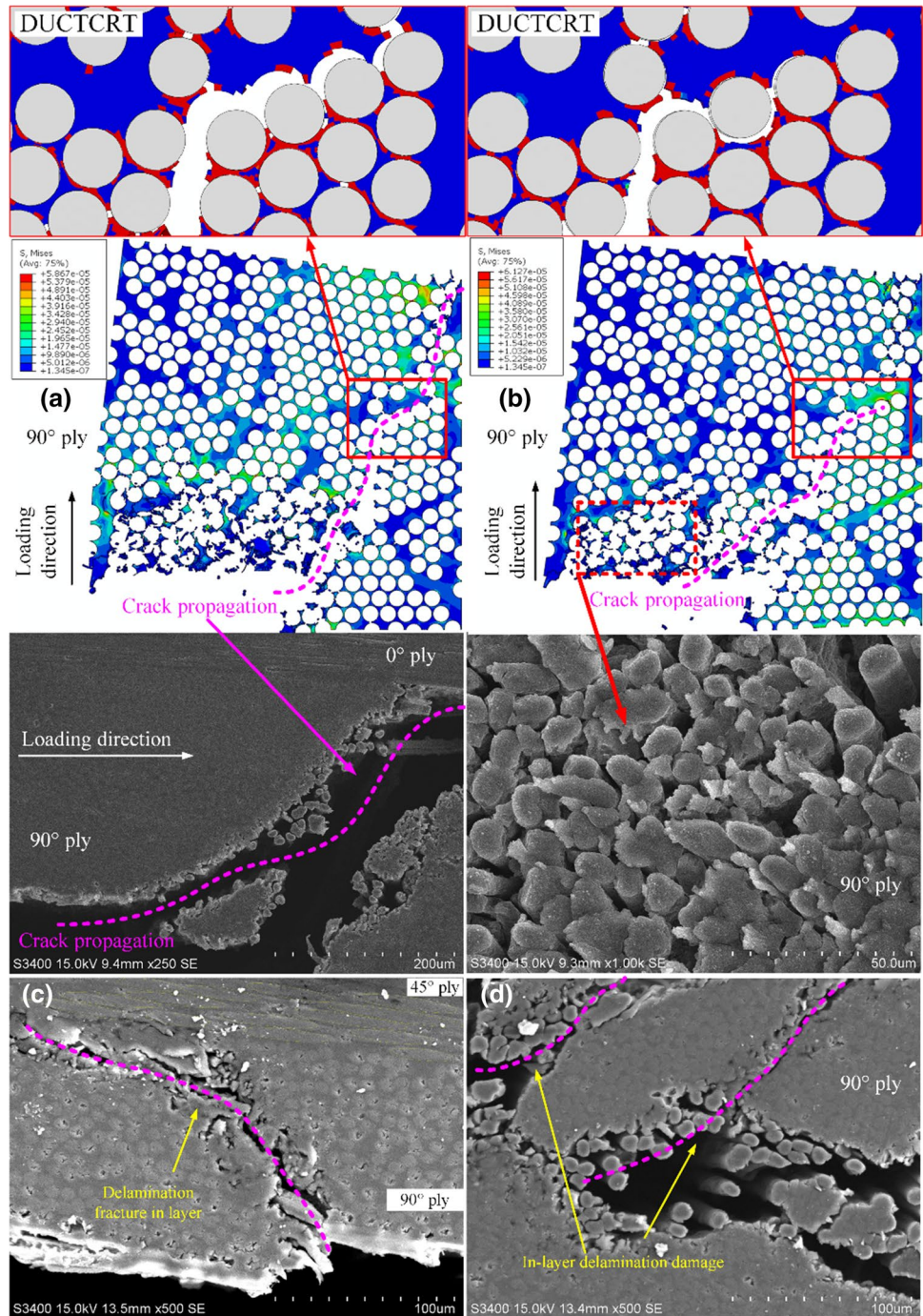
It is essential to simulate the potential damage that may occur during exposure to low temperatures in order to comprehensively investigate the influence of residual stress on the material. The objective of this study is to examine the mechanism of damage initiation in CFRP joints under low-temperature conditions. When subject to tensile loading, the CFRP experiences compression from the bolt-shank against the hole wall. As a result of the varying stiffness of the interference joints after exposure to low temperatures, the displacement during the load-bearing process differs. A smaller deformation around the hole is observed when the stiffness is greater. Therefore, the damage behavior of the RVEs model can be evaluated by controlling the displacement variation, which can be understood by comparing experimental results obtained at different temperatures. According to results in the current literature [37], the joint exhibits initial damage in the 90° ply at room temperature. Our experimental observations also indicate that under low-temperature conditions, the same damage occurs first at the 90° lay.

The damage in the 90° ply experienced by the CFRP is illustrated in Fig. 11, where it is observed to initiate from areas of high fiber density with weak adhesion between the fibers and the resin, regardless of whether at room temperature or low temperature. During compression, the resin matrix is the first sustain damage due to its significantly lower strength compared to the fibers. In this model, the resin matrix elements are deleted when the stress exceeds their strength, resulting in the formation of microcracks. These microcracks converge and form a main crack. As

depicted in Fig. 11, the main crack propagates along a 60° direction at ambient temperatures; while at low temperatures, it propagated along a 45° direction. Concurrent with crack propagation, microcracks are also formed in regions with small spacing between fibers, causing continuous destruction of the matrix. Finally, the crack extends into the interface layer, leading to delamination failure.

The RVE model reveals that the primary failure modes in the early stages of damage are matrix compression fracture and fiber-matrix interface debonding, while fiber breakage

**Fig. 11** Initial damage morphology during the tensile loading of the CFRP for 90° ply; results obtained at temperatures of **a** 20 °C and **b, c, d** -40 °C



does not occur during the initial damage stages. SEM images further confirm the accuracy of the model in capturing the damage behavior along the main crack.

Moreover, Fig. 11c, d shows delamination and in-layer delamination damage within the 90° ply also occur at low temperatures. This phenomenon can be attributed to the enhanced bonding strength between the fibers and matrix under low temperature, leading to the occurrence of in-layer delamination and subsequent fibers bundling. Additionally, as depicted in Fig. 11c, It can be observed that although a large crack has been formed between the 90° ply direction, there is almost no significant damage in the 45° ply direction during the damage initiation stage.

Due to the utilization of the interference fit technique and the application of a high tightening torque (4 Nm), the axial displacement of the CFRP is constrained during tension.

As a result, in the early stages of damage, the joints exhibit a failure mode characterized by compression of the bolt shank against the CFRP hole wall, as depicted in Fig. 12. Conversely, in the 0° ply orientation, the load-bearing process initiates with fibers micro-buckling. This phenomenon arises from localized regions where the bonding between the fibers and matrix is weak, leading to debonding caused by stress concentration. This debonding creates voids that accommodate fibers micro-buckling. However, the limitations imposed on axial displacement impede further bending of the fibers. As the applied load increases, the matrix undergoes preferential compression failure, eventually leading to fracture of the fibers when the local interfacial shear stress exceeds their carrying capacity.

As tension progresses and further compresses the CFRP, secondary fractures occur in 0° ply direction, as shown in

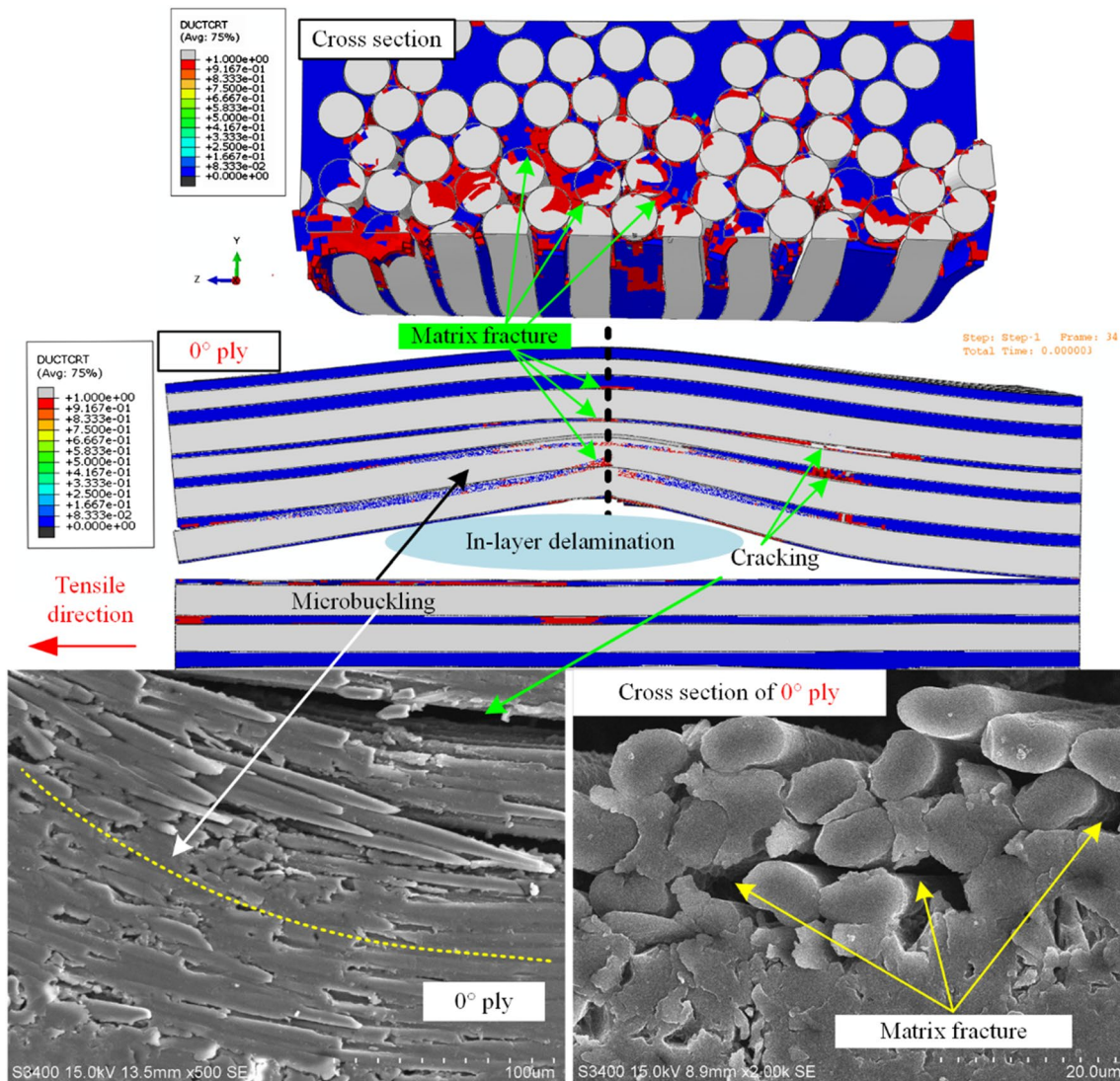


Fig. 12 Damage initiation of CFRP in 0° ply direction

**Fig. 13** Damage propagation of CFRP in  $0^\circ$  ply direction

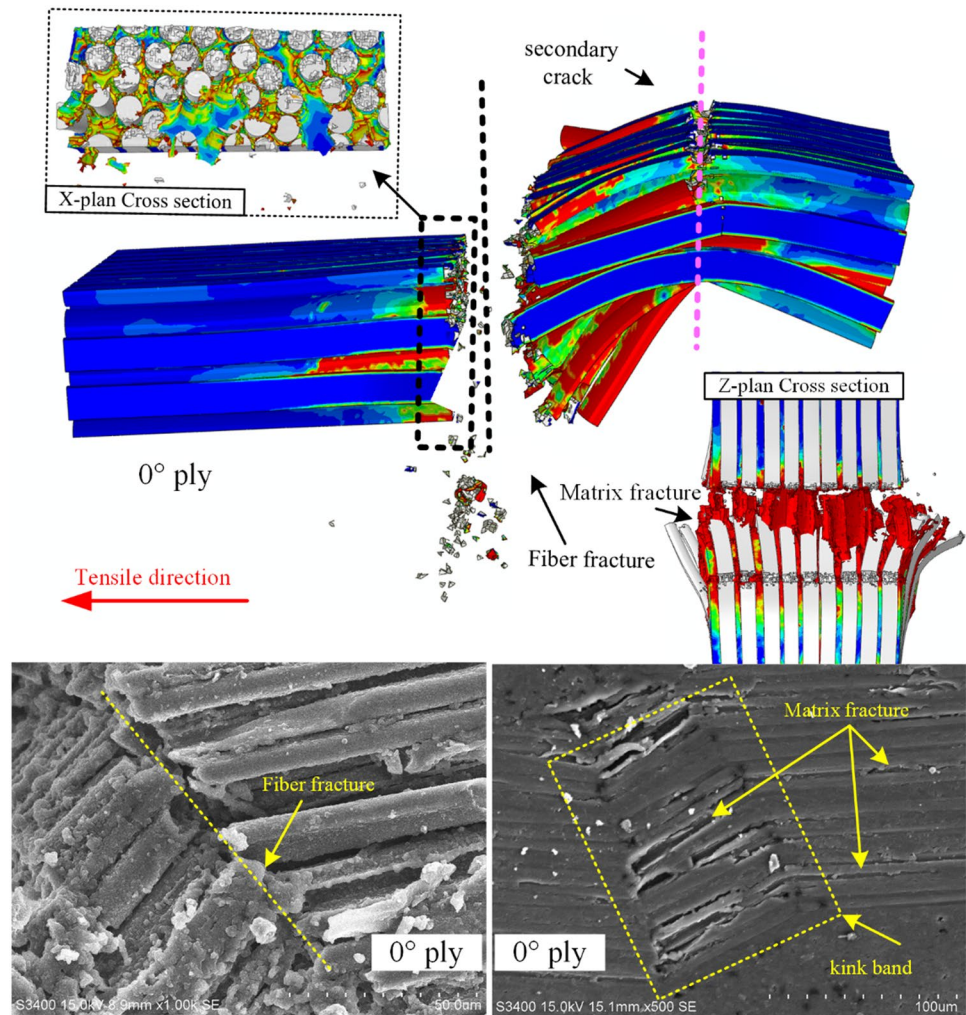


Fig. 13, leading to the formation of numerous kink bands in the  $0^\circ$  ply orientation until ultimate failure. We propose that the formation of kink bands at low temperatures is attributed to stress concentration in specific areas, such as fiber-dense regions and interlaminar regions, and the preferential occurrence of cracking during the load-bearing process. These cracks create micropores that allow for the formation of kink bands.

During the initial stages of damage, it is important to note that the  $90^\circ$  ply orientation experiences predominant failure within the limited load-bearing space, while kink band damage in the  $0^\circ$  orientation occurs only in localized regions. In the  $0^\circ$  ply orientation, the primary mechanisms of damage during the damage initiation stage include matrix compression failure, fiber micro-buckling, and kink bands.

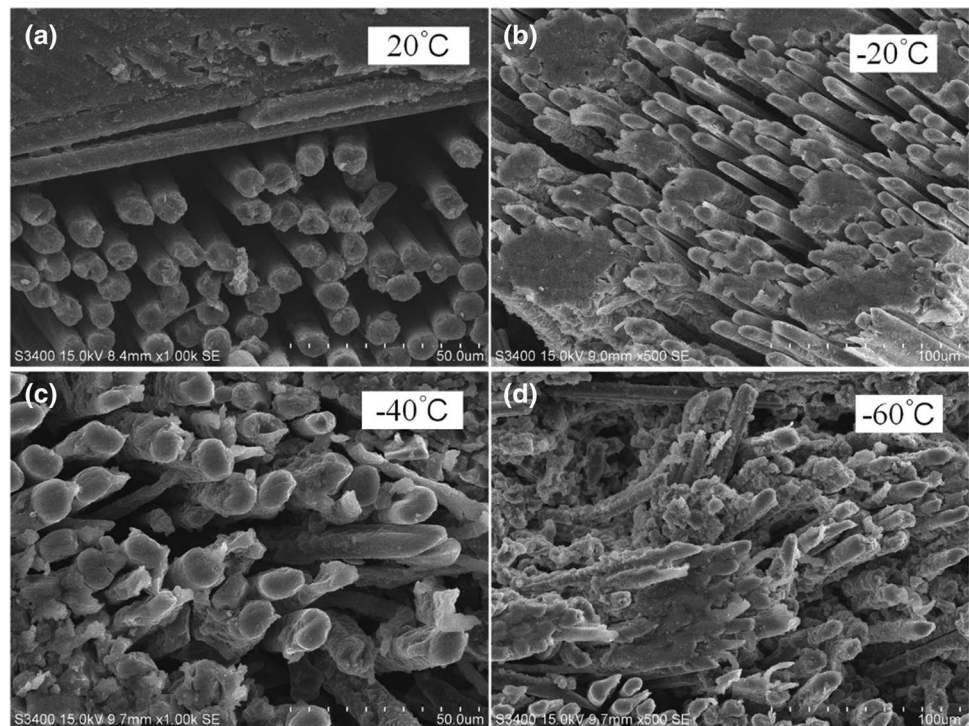
The failure morphology of the specimens at ambient temperature is shown in Fig. 14a, exhibiting a relatively clean surface of fibers. The failure is characterized by smooth fibers and no residual resin can be seen bonded to

the surface of the fibers. This observation indicates that the final failure of the specimen is primarily attributable to the peeling between the resin matrix and fibers, resulting in fibers fracture under external force.

After long-term low-temperature exposure, the adhesion between the resin and fiber surface is stronger than at ambient temperatures in Fig. 14b, c, d. For example, at  $-60^\circ\text{C}$ , some resin remains adhered to the fibers after failure, indicating a strong bonding between the fiber and resin in the specimens exposed to low temperatures. This improved adhesion between the fibers and the resin also confirms that a low-temperature treatment will enhance the strength and stiffness of the joint.

Additionally, the fibers aggregate into bundles at the fracture surface of the specimen exposed to low temperatures. The failure of this specimen is primarily due to peeling between the matrix and the fiber, shear failure of the inter-fiber/resin matrix, and the fracture of the fiber bundles.

**Fig. 14** Fracture morphology of the CFRP at different temperatures, **a** 20 °C, **b** –20 °C, **c** –40 °C, and **d** –60 °C



## 5 Conclusion

This work investigated the mechanical performances of CFRP interference-fit bolted joints subjected to low-temperature exposure. The tensile strength, stiffness, thermal residual stress, and failure models were analyzed through experiments and 3D-RVEs models. The key findings are as follows:

- (1). Appropriate interference fits and low-temperature exposure can improve the tensile strength and stiffness of the examined joints. As the interference-fit sizes increase, the strength and stiffness of the joints initially increase before decreasing after long-term low-temperature exposure. Joints with an interference fit of 1.64% exhibit the highest ultimate tensile strength and stiffness. The strength and stiffness of the joints demonstrate an approximately linear increase with decreasing temperature.
- (2). The strength and stiffness of CFRP bolted joints initially increase and then decrease with increasing exposure time to a given low temperature. The initial increase is attributed to the enhanced bonding between the matrix and fibers due to matrix shrinkage after low-temperature exposure, as well as better fibers support. The subsequent decrease occurs because prolonged low-temperature exposure leads to resin shrinkage within the CFRP reaching a point where the stress generated by the resin resistance to shrinkage

may exceed the bonding strength between the resin and the fibers, resulting in the microcracks caused by debonding. Under tensile load, the rapid expansion of cracks leads to delamination damage within the material, thereby reducing its load transfer capacity and strength.

- (3). Low-temperature exposure generates thermal residual stresses within the CFRP due to the difference in the thermal expansion coefficients of the fiber and the resin. The presence of thermal residual stress influences the cracks propagation path when it is subjected to its failure load, and the failure mechanisms of different ply orientations in CFRP are also different. Co-shrinkage of the resin-wrapped fiber also occurs due to low-temperature exposure, enhancing the cohesion between the fibers and resin.

**Acknowledgements** The authors would like to acknowledge the editors and the anonymous reviewers for their insightful comments. This research is supported by the Natural Science Foundation of Fujian Province, China (2021J011089). We also acknowledge that part of the contributions for this research was funded and supported by the Central Government Guided Local Science and Technology Development Fund Project, China (2022ZY1026)

## Declarations

**Conflict of interest** The authors declared no potential conflicts of interest with respect to the research, authorship, and/or publication of this article.



## References

- Zhang J, Rao J, Ma L, Wen X (2022) Investigation of the damping capacity of CFRP raft frames. *Materials* 15(2):653
- Altin M, Motorcu AR, Gökkaya H (2020) Optimization of machining parameters for kerf angle and roundness error in abrasive water jet drilling of CFRP composites with different fiber orientation angles. *J Braz Soc Mech Sci* 42:173
- Sethi S, Ray BC (2015) Environmental effects on fibre reinforced polymeric composites: evolving reasons and remarks on interfacial strength and stability. *Adv Colloid Interface Sci* 217:43–67
- Mára V, Michalcová L, Kadlec M, Krčil J, Špatenka P (2021) The effect of long-time moisture exposure and low temperatures on mechanical behavior of open-hole Cfrp laminate. *Polym Composite* 42(7):3603–3618
- Liu Y, Wang M, Tian W, Qi B, Lei Z, Wang W (2019) Ohmic heating curing of carbon fiber/carbon nanofiber synergistically strengthening cement-based composites as repair/reinforcement materials used in ultra-low temperature environment. *Compos Part A Appl Sci Manuf* 125:105570
- Hu Y, Cheng F, Ji Y, Yuan B, Hu X (2020) Effect of aramid pulp on low temperature flexural properties of carbon fibre reinforced plastics. *Compos Sci Technol* 192:108095
- Ge J, Cheng G, Su Y, Zou Y, Ren C, Qin X, Wang G (2022) Effect of cooling strategies on performance and mechanism of helical milling of CFRP/Ti–6Al–4V stacks. *Chin J Aeronaut* 35(2):388–403
- Zaoutsos S, Zilidou M (2017) Influence of extreme low temperature conditions on the dynamic mechanical properties of carbon fiber reinforced polymers. *IOP Conf Ser Mater Sci Eng* 276:012024
- Wilson PR, Cinar AF, Mostafavi M, Meredith J (2018) Temperature driven failure of carbon epoxy composites—a quantitative full-field study. *Compos Sci Technol* 155:33–40
- Dutta P, Hui D (1996) Low-temperature and freeze-thaw durability of thick composites. *Compos Part B Eng* 27(3–4):371–379
- Takeda T, Shindo Y, Narita F (2012) Three-dimensional stress analysis of cracked satin woven carbon fiber reinforced/polymer composites under tension at cryogenic temperature. *Jpn Soc Mech Eng* 47:84–85
- Wei Z, Takeda T, Narita F, Shindo Y (2014) Flexural fatigue performance and electrical resistance response of carbon nanotube-based polymer composites at cryogenic temperatures. *Cryogenics* 59:44–48
- Liu PF, Liao BB, Jia LY, Peng XQ (2016) Finite element analysis of dynamic progressive failure of carbon fiber composite laminates under low velocity impact. *Compos Struct* 149:408–422
- Zhao Y, Chen Y, Ai S, Fang D (2019) A diffusion, oxidation reaction and large viscoelastic deformation coupled model with applications to SiC fiber oxidation. *Int J Plast* 118:173–189
- Yan M, Jiao W, Yang F, Ding G, Zou H, Xu Z, Wang R (2019) Simulation and measurement of cryogenic-interfacial-properties of T700/modified epoxy for composite cryotanks. *Mater Des* 182:108050
- Ren M, Zhang X, Huang C, Wang B, Li T (2019) An integrated macro/micro-scale approach for in situ evaluation of matrix cracking in the polymer matrix of cryogenic composite tanks. *Compos Struct* 216:201–212
- Meng J, Wang Y, Yang H, Wang P, Lei Q, Shi H, Lei H, Fang D (2020) Mechanical properties and internal microdefects evolution of carbon fiber reinforced polymer composites: cryogenic temperature and thermocycling effects. *Compos Sci Technol* 191:108083
- Wu Q, Ogasawara T, Yoshikawa N, Zhai H (2018) Stress evolution of amorphous thermoplastic plate during forming process. *Materials* 11(4):464
- Wu Q, Zhai H, Yoshikawa N, Ogasawara T (2020) Localization simulation of a representative volume element with prescribed displacement boundary for investigating the thermal residual stresses of composite forming. *Compos Struct* 235:111723
- Wu Q, Yoshikawa N, Zhai H (2020) Composite forming simulation of a three-dimensional representative model with random fiber distribution. *Comput Mater Sci* 182:109780
- Solati A, Hamed M, Safarabadi M (2019) Combined GA-ANN approach for prediction of HAZ and bearing strength in laser drilling of GFRP composite. *Opt Laser Technol* 113:104–115
- Solati A, Hamed M, Safarabadi M (2019) Comprehensive investigation of surface quality and mechanical properties in CO<sub>2</sub> laser drilling of GFRP composites. *Int J Adv Manuf Tech* 102:791–808
- Nazari F, Safarabadi M (2018) Experimental and numerical investigation of loading speed effect on the bearing strength of glass/epoxy composite joints. *Compos Struct* 195:211–218
- Yang L, Li Z, Xu H, Wu Z (2019) Prediction on residual stresses of carbon/epoxy composite at cryogenic temperature. *Polym Compos* 40:3412–3420
- Hu J, Zhang K, Cheng H, Qi Z (2020) Mechanism of bolt pretightening and preload relaxation in composite interference-fit joints under thermal effects. *J Compos Mater* 54(30):002199832094121
- Li J, Lai X, Zou P, Guo W, Tang C (2021) Effect of imbalanced interface pre-tightening force on the bearing behavior of carbon fiber reinforced polymer interference-fit lap joint. *Adv Mech Eng* 13(4):1–13
- Zuo Y, Yue T, Jiang R, Cao Z, Yang L (2022) Bolt insertion damage and mechanical behaviors investigation of CFRP/CFRP interference fit bolted joints. *Chin J Aeronaut* 35(9):354–365
- Klinkova O, Rech J, Drapier S, Bergheau J (2011) Characterization of friction properties at the workmaterial/cutting tool interface during the machining of randomly structured carbon fibers reinforced polymer with carbide tools under dry conditions. *Tribol Int* 44(12):2050–2058
- Chardon G, Klinkova O, Rech J, Drapier S, Bergheau J (2015) Characterization of friction properties at the work material/cutting tool interface during the machining of randomly structured carbon fibers reinforced polymer with poly crystalline diamond tool under dry conditions. *Tribol Int* 81:300–308
- Schön J (2000) Coefficient of friction of composite delamination surfaces. *Wear* 237(1):77–89
- Belingardi G, Mehdipour H, Mangino E, Martorana B (2016) Progressive damage analysis of a rate-dependent hybrid composite beam. *Compos Struct* 154:433–442
- Cheng H, Gao J, Kafka OL, Zhang K, Luo B, Liu W (2017) A micro-scale cutting model for UD CFRP composites with thermo-mechanical coupling. *Compos Sci Technol* 153:18–31
- Naik N, Shankar P, Kavala V, Ravikummar G, Pothnis J, Arya H (2011) High strain rate mechanical behavior of epoxy under compressive loading: experimental and modeling studies. *Mater Sci Eng A Struct* 528(3):846–854
- Yan X, Reiner J, Bacca M, Altintas Y, Vaziri R (2019) A study of energy dissipating mechanisms in orthogonal cutting of UD-CFRP composites. *Compos Struct* 220:460–472
- Benzezaggh M, Kenane M (1996) Measurement of mixed-mode delamination fracture toughness of unidirectional glass/epoxy composites with mixed-mode bending apparatus. *Compos Sci Technol* 56(4):439–449
- Wu Y, Chen M, Chen M, Ran Z, Zhu C, Liao H (2017) The reinforcing effect of polydopamine functionalized graphene

- nanoplatelets on the mechanical properties of epoxy resins at cryogenic temperature. *Polym Test* 58:262–269
37. Zou P, Chen X, Chen H, Xu G (2020) Damage propagation and strength prediction of a single-lap interference-fit laminate structure. *Front Mech Eng* 15(4):558–570

Springer Nature or its licensor (e.g. a society or other partner) holds exclusive rights to this article under a publishing agreement with the author(s) or other rightsholder(s); author self-archiving of the accepted manuscript version of this article is solely governed by the terms of such publishing agreement and applicable law.

**Publisher's Note** Springer Nature remains neutral with regard to jurisdictional claims in published maps and institutional affiliations.